

PAPER: Quantum statistical physics, condensed matter, integrable systems

# Dynamics of longitudinal magnetization in transverse-field quantum Ising model: from symmetry-breaking gap to Kibble–Zurek mechanism

Michał Białończyk and Bogdan Damski

Jagiellonian University, Marian Smoluchowski Institute of Physics,  
Łojasiewicza 11, 30-348 Kraków, Poland  
E-mail: [bogdan.damski@uj.edu.pl](mailto:bogdan.damski@uj.edu.pl)

Received 8 October 2019

Accepted for publication 26 November 2019

Published 27 January 2020



Online at [stacks.iop.org/JSTAT/2020/013108](https://stacks.iop.org/JSTAT/2020/013108)  
<https://doi.org/10.1088/1742-5468/ab609a>

**Abstract.** We show that the symmetry-breaking gap of the quantum Ising model in the transverse field can be extracted from free evolution of the longitudinal magnetization taking place after a gradual quench of the magnetic field. We perform for this purpose numerical simulations of the Ising chains with either periodic or open boundaries. We also study the condition for adiabaticity of evolution of the longitudinal magnetization finding excellent agreement between our simulations and the prediction based on the Kibble–Zurek theory of non-equilibrium phase transitions. Our results should be relevant for ongoing cold atom and ion experiments targeting either equilibrium or dynamical aspects of quantum phase transitions. They could be also useful for benchmarking D-Wave machines.

**Keywords:** quantum quenches

J. Stat. Mech. (2020) 013108

## Contents

<b>1. Introduction</b>	<b>2</b>
<b>2. Idea</b>	<b>3</b>
<b>3. Two spins</b>	<b>7</b>
<b>4. Dynamics of periodic chains</b>	<b>9</b>
<b>5. Dynamics of chains with open boundaries</b>	<b>12</b>
5.1. Quenches stopping in ferromagnetic or paramagnetic phase .....	14
5.2. Quenches to critical point.....	15
<b>6. Discussion</b>	<b>21</b>
<b>Acknowledgments</b> .....	<b>22</b>
<b>Appendix A. Longitudinal magnetization in Jordan–Wigner- transformed periodic Ising chains</b> .....	<b>22</b>
<b>Appendix B. Diagonalization and time evolution of Ising chains with open boundaries</b> .....	<b>24</b>
B.1. Diagonalization .....	24
B.2. Equilibrium longitudinal magnetization.....	25
B.3. Time evolution.....	25
<b>References</b>	<b>26</b>

---

## 1. Introduction

Quantum phase transitions take place when tiny changes of the external parameter, such as the magnetic field in spin models or the lattice height in cold atom setups, can induce radical changes in ground state properties of the system [1–4]. This can happen when the system is near the critical point separating its phases.

One of the typical features associated with quantum phase transitions is the symmetry-breaking phenomenon, where one of the phases of the thermodynamically-large system has degenerate ground states, which do not respect the symmetry of the Hamiltonian. Such a degeneracy is typically lifted in finite systems, where a small energy gap between lowest-energy eigenstates of the Hamiltonian is present. Rapid disappearance of this gap with increase of the system size signals the onset of the symmetry-breaking phenomenon that is fundamentally important for understanding of both equilibrium and non-equilibrium phase transitions. It is thus very interesting to address the question how one can access the symmetry-breaking gap in real systems to observe emergence of such a compelling phenomenon.

We make a step forward in this direction by providing an explicit two-stage scheme for studies of the symmetry-breaking gap in the paradigmatic system undergoing a quantum phase transition: the quantum Ising model in the transverse magnetic field

[1]. In the first stage, the system is gradually driven to the desired value of the transverse magnetic field (see [5–22] for studies of different aspects of dynamics of the quantum Ising model under similar driving). In the second stage, the system undergoes free evolution and oscillations of its longitudinal magnetization are recorded. They encode the symmetry-breaking gap.

While our studies target a specific model, we expect that they can be generalized to other, not necessarily exactly solvable systems, which can be experimentally approached in cold atom and ion simulators of various condensed matter models [4, 23]. In fact, while pursuing this work, we have come across a recent paper discussing experimental studies of the symmetry-breaking gap in a cold atom cloud [24]. We will first present our results and then compare the two approaches.

The outline of this paper is the following. We explain the idea behind our work in section 2. We illustrate in section 3 the concepts related to the symmetry-breaking gap and the equilibrium longitudinal magnetization in the simplest version of the Ising model composed of just two spins. We then discuss in section 4 dynamical extraction of those quantities from after-quench free evolution of the longitudinal magnetization in the periodic Ising chain composed of several spins. Next, we extend these studies in section 5 to systems composed of up to several hundreds of spins by considering Ising chains with open boundaries, where computations of the longitudinal magnetization can be more efficiently done. The overall discussion of our results is presented in section 6. Finally, technicalities related to the studies of the Ising chains with either periodic or open boundaries are presented in appendices A and B.

## 2. Idea

To explain the idea behind our proposal, we introduce the quantum Ising model in the transverse magnetic field  $g$ , whose Hamiltonian in the periodic chain can be written as [25]

$$H(g) = - \sum_{i=1}^N (\sigma_i^x \sigma_{i+1}^x + g \sigma_i^z)$$

$$\sigma_{N+1}^x = \sigma_1^x \tag{1}$$

where  $\sigma_j^{x,y,z}$  is the Pauli matrix acting on the  $j$ th spin,  $N$  is the number of spins, and  $g \geq 0$  is assumed in this work. Such a model has two phases: the ferromagnetic phase for  $0 \leq g < 1$  and the paramagnetic phase for  $g > 1$ . The breaking of the  $\mathbb{Z}_2$  symmetry of this model, associated with the  $\sigma_j^x \rightarrow -\sigma_j^x$  symmetry of the Hamiltonian, can be easily explained at  $g = 0$ , when the two ground states have all spins aligned in the  $\pm x$  direction

$$| \rightarrow \rightarrow \rightarrow \dots \rangle, | \leftarrow \leftarrow \leftarrow \dots \rangle. \tag{2}$$

Then an arbitrarily small perturbation along the  $x$  direction, say  $-h \sum_i \sigma_i^x$  with  $h \rightarrow 0^+$ , makes  $| \rightarrow \rightarrow \rightarrow \dots \rangle$  the ground state of the system breaking the spin-flip symmetry supported by the Hamiltonian. Importantly, degeneracy of the ground state, in thermodynamically-large systems, persists in the whole ferromagnetic phase.

The idea that we have is that one can initially set  $g = 0$  and prepare the system in one of the states given in (2), say

$$|\psi\rangle = |\rightarrow\rightarrow\rightarrow\cdots\rangle. \tag{3}$$

We propose then to evolve the system according to the following protocol

$$g(t) = \begin{cases} g_f + t/\tau_Q & \text{for } -g_f\tau_Q \leq t \leq 0 \\ g_f & \text{for } t > 0 \end{cases} \tag{4}$$

with  $\tau_Q$  controlling the rate of driving the system to the magnetic field  $g_f$ , where free evolution begins.

The natural observable for studies of the symmetry-breaking gap is the longitudinal magnetization

$$M_x = \langle \sigma_i^x \rangle, \tag{5}$$

where the choice of the site index  $i$  is arbitrary in a periodic chain. Such an observable is sensitive to the way in which the symmetry is broken. Indeed, it is well known that

$$-M_x^{\text{eq}} \leq M_x \leq M_x^{\text{eq}}, \tag{6}$$

where in the thermodynamically-large system [26]

$$M_x^{\text{eq}} = \begin{cases} (1 - g^2)^{1/8} & \text{for } 0 \leq g \leq 1 \\ 0 & \text{for } g > 1 \end{cases}. \tag{7}$$

$M_x^{\text{eq}}$  will be called the equilibrium longitudinal magnetization. It was obtained in the  $N \rightarrow \infty$  limit from the asymptotic form of the two-point correlation functions. We will study it in finite systems, where a different approach has to be employed (see below). Typical results that we obtain are illustrated in figure 1, where we see that  $M_x^{\text{eq}}$  is analytic when  $N < \infty$ . In such systems, the drop of the longitudinal magnetization is not as steep as in (7) on the ferromagnetic side. On the paramagnetic side, non-zero value of  $M_x^{\text{eq}}$  appears—see (27) and discussion around it.

The question now is how the symmetry-breaking gap can be extracted from dynamics of the longitudinal magnetization. To explain that, we first note that the expectation value of the  $\sigma_j^x$  operator vanishes in all eigenstates of Hamiltonian (1) for  $g > 0$ . This can be proved with Wick’s theorem [27] in the fermionic representation of the Ising model, which we briefly introduce in appendix A. Non-zero value of the longitudinal magnetization can be obtained by evaluation of (5) in a proper superposition of two eigenstates of the Hamiltonian. In fact, deceptively simple-looking initial state (3) is a macroscopic superposition of two eigenstates belonging to different sectors of the spectrum of Hamiltonian (1).

To understand this statement, we note that Hamiltonian (1) commutes with the parity operator,

$$P = \prod_{i=1}^N \sigma_i^z, \quad [H, P] = 0. \tag{8}$$

This leads to splitting of the Hilbert space into two subspaces, where the eigenstates have either  $+1$  or  $-1$  parity [28]. The symmetry-breaking gap  $\delta$  is the difference between the energies of the lowest-energy eigenstates in the negative and positive parity subspaces

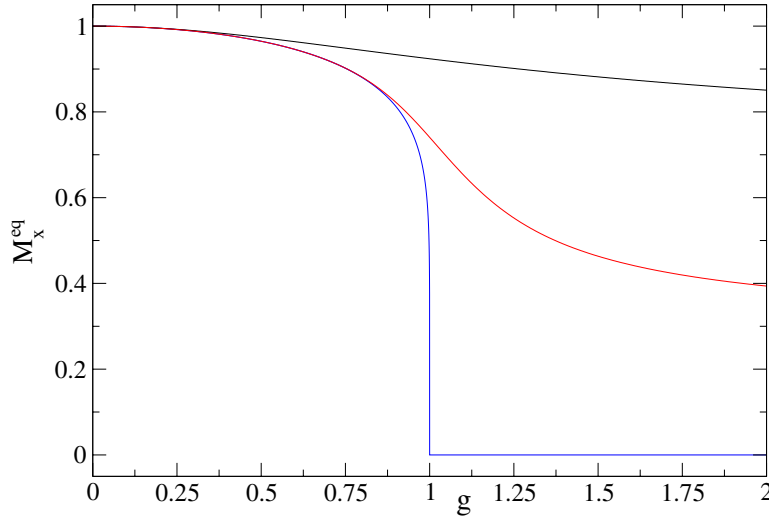


**Figure 1.** The equilibrium longitudinal magnetization  $M_x^{\text{eq}}$  of periodic Ising chains. The curves, top to bottom, correspond to system sizes 2 (black), 12 (red), and  $\infty$  (blue). The first of them comes from (26), the second one has been numerically obtained through exact diagonalization, the last one is given by (7).

in the ferromagnetic phase, where the symmetry-breaking phenomenon takes place. Such a quantity, however, will be of key importance in our studies for any value of the magnetic field  $g$ . We will thus call it the symmetry-breaking gap even when it will be computed at the critical point or in the paramagnetic phase, which will simplify our discussion.

These features of the spectrum are illustrated in figure 2. A closed-form expression for  $\delta$  was given in [28]

$$\delta = g^N \int_0^1 dt \frac{4N t^{N-3/2} \sqrt{(1-t)(1-g^2t)}}{\pi (1-(gt)^{2N})} \text{ for } 0 \leq g < 1, \quad (9)$$

$$\delta = 2g - 2 + g^{-N} \int_0^1 dt \frac{4N t^{N-3/2} \sqrt{(1-t)(g^2-t)}}{\pi (1-t^{2N}/g^{2N})} \text{ for } g > 1, \quad (10)$$

$$\delta = 2 \tan\left(\frac{\pi}{4N}\right) \text{ at } g = 1. \quad (11)$$

These expressions can be used for showing that  $\delta$  vanishes exponentially (algebraically) with the system size deeply in the ferromagnetic phase (near the critical point) [28]. Deeply in the paramagnetic phase,  $\delta$  is well-approximated by an expression that is obtained from (10) after neglecting the term containing the integral.

Besides the symmetry-breaking gap, there are also dynamical gaps  $\Delta_+$  and  $\Delta_-$ . They are defined as energy gaps in subspaces of positive and negative parity between the ground state and the first excited state that can be populated during evolution starting from (3)—see figure 2. Their importance comes from the fact that commutation relation (8) prohibits dynamical transitions between the two parity subspaces. As a result, system’s excitation due to driving (4) depends on  $\Delta_{\pm}$ , the quench time  $\tau_Q$ , and the initial state (3) for time evolution. It has nothing to do with the symmetry-breaking

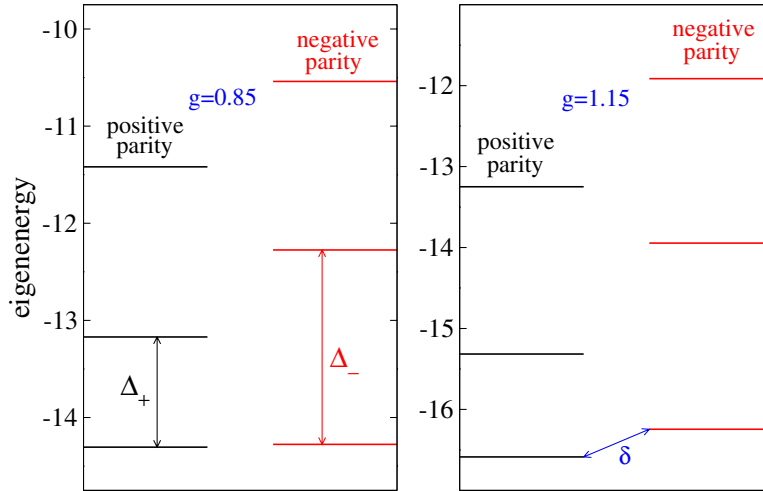


**Figure 2.** Lowest-energy levels of Hamiltonian (1) for  $N = 12$ , which are populated during time evolution starting from state (3) and driven by quench protocol (4). Left panel: typical results in the ferromagnetic phase. The positive and negative parity ground states are nearly degenerate despite the relatively small system size. Right panel: typical results in the paramagnetic phase. The dynamical gaps in the positive and negative parity subspaces,  $\Delta_+$  and  $\Delta_-$ , respectively, and the symmetry-breaking gap  $\delta$  are marked to illustrate key quantities involved in our studies. Their values for the parameters used in this figure can be found in table 1.

**Table 1.** The symmetry-breaking gap  $\delta$ , the dynamical gaps  $\Delta_{\pm}$ , and the equilibrium longitudinal magnetization  $M_x^{\text{eq}}$  in the periodic Ising chain composed of  $N = 12$  spins. The first column is obtained from (9)–(11), the next two columns come from (A.11), the fourth column is numerically obtained through exact diagonalization.

	$\delta$	$\Delta_+$	$\Delta_-$	$M_x^{\text{eq}}$
$g = 0.85$	0.028 747	1.13	2.00	0.8545
$g = 1$	0.131 09	1.04	2.07	0.7407
$g = 1.15$	0.341 67	1.27	2.30	0.6146

gap  $\delta$  as long as there is no symmetry-breaking perturbation in the system, which is the case in our studies.

If we now note that  $\sigma^z|\rightarrow\rangle = |\leftarrow\rangle$ , which implies  $\sigma^z|\leftarrow\rangle = |\rightarrow\rangle$ , we see that the ground states in the positive and negative parity subspaces at  $g = 0$  can be written as

$$|GS_{\pm}(g = 0)\rangle = \frac{|\rightarrow\rightarrow\rightarrow\cdots\rangle \pm |\leftarrow\leftarrow\leftarrow\cdots\rangle}{\sqrt{2}}, \tag{12}$$

which in turn allows us to cast initial state (3) to the following form

$$|\psi\rangle = \frac{|GS_+(g = 0)\rangle + |GS_-(g = 0)\rangle}{\sqrt{2}}. \tag{13}$$

Next, we use (8) and employ time-dependent Schrödinger equation to arrive at

$$|\psi(t)\rangle = |\psi_+(t)\rangle + |\psi_-(t)\rangle, \tag{14}$$

$$P|\psi_{\pm}(t)\rangle = \pm|\psi_{\pm}(t)\rangle.$$

Finally, knowing that  $\sigma_i^x$  has vanishing matrix elements in the positive and negative parity subspaces, which can be easily proven with the help of Wick’s theorem, we get

$$M_x(t) = \langle \psi(t) | \sigma_i^x | \psi(t) \rangle = \langle \psi_-(t) | \sigma_i^x | \psi_+(t) \rangle + \text{c.c.} \quad (15)$$

This expression can be very complicated for fast quenches, i.e. for small  $\tau_Q$  in (4). However, if we assume that the driving is slow enough to be nearly adiabatic, then the following expression will properly approximate the exact result

$$M_x(t) = \cos\left(\int_{-g_f\tau_Q}^t dt \delta[g(t)]\right) \langle GS_-[g(t)] | \sigma_i^x | GS_+[g(t)] \rangle. \quad (16)$$

Such an expression is still non-trivial because we are unaware of a closed-form expression for the above matrix element in an arbitrarily-sized system. If we now consider  $t > 0$ , i.e. the free evolution stage in our problem, we will get from (16) that

$$M_x(t) = \cos(\delta(g_f)t + \text{const}) M_x^{\text{eq}}(g_f), \quad (17)$$

which can be used for extracting the symmetry-breaking gap and the equilibrium longitudinal magnetization out of either numerical or experimental data.

The question now is what is the condition for adiabaticity in our system so that approximation (16) can be used. Clearly, the system is most prone to being excited near the critical point, where the dynamical gap  $\Delta_{\pm}$  is smallest, and the quantum version [5, 6, 29] of the Kibble–Zurek (KZ) theory of non-equilibrium phase transitions [30–33] can be used. A simple criteria then exists and is based on comparison between the system size and the non-equilibrium length-scale  $\hat{\xi}$  characterizing excitations resulting from the quench [34]. The latter, according to the KZ theory, scales with the quench time as

$$\hat{\xi} \sim \tau_Q^{\nu/(1+z\nu)}, \quad (18)$$

where  $z$  and  $\nu$  are the critical exponents. These exponents describe disappearance of the dynamical gap and the correlation length, which are assumed to be proportional to  $|g - g_c|^{z\nu}$  and  $|g - g_c|^{-\nu}$ , respectively, near the critical point  $g_c$ . Comparing the two length scales, one gets the following condition for a crossover between adiabatic and non-adiabatic evolutions approaching or crossing the critical point

$$\tau_Q \sim N^{(1+z\nu)/\nu} \sim N^2, \quad (19)$$

where we substituted  $z = \nu = 1$  for the quantum Ising model in the transverse field. In other words, for quench times of the order of  $N^2$  or larger we expect the evolution to be nearly adiabatic.

### 3. Two spins

We illustrate here the quantities introduced in the previous section by showing how the symmetry-breaking gap and the longitudinal magnetization can be calculated in the simplest version of the Ising chain, the one with just two spins.

To start, we need eigenenergies and normalized eigenstates of (1), which for  $N = 2$  read

$$\mathcal{E}_{GS_+} = -2\sqrt{1+g^2}, \quad |GS_+\rangle = A_-|\uparrow\uparrow\rangle + B_-|\downarrow\downarrow\rangle, \tag{20}$$

$$\mathcal{E}_{GS_-} = -2, \quad |GS_-\rangle = \frac{|\uparrow\downarrow\rangle + |\downarrow\uparrow\rangle}{\sqrt{2}}, \tag{21}$$

$$\mathcal{E}_{EX_-} = 2, \quad |EX_-\rangle = \frac{|\uparrow\downarrow\rangle - |\downarrow\uparrow\rangle}{\sqrt{2}}, \tag{22}$$

$$\mathcal{E}_{EX_+} = 2\sqrt{1+g^2}, \quad |EX_+\rangle = A_+|\uparrow\uparrow\rangle + B_+|\downarrow\downarrow\rangle, \tag{23}$$

where  $\sigma^z|\uparrow\rangle = |\uparrow\rangle, \sigma^z|\downarrow\rangle = -|\downarrow\rangle,$

$$A_{\pm} = \frac{1}{\sqrt{2}\sqrt{1+g^2 \pm g\sqrt{1+g^2}}}, \quad B_{\pm} = -\frac{g \pm \sqrt{1+g^2}}{\sqrt{2}\sqrt{1+g^2 \pm g\sqrt{1+g^2}}}, \tag{24}$$

and  $EX_{\pm}$  refers to the excited states in the corresponding subspaces.

Using these results, one immediately gets

$$\delta = \mathcal{E}_{GS_-} - \mathcal{E}_{GS_+} = 2\left(\sqrt{1+g^2} - 1\right), \tag{25}$$

which agrees with (9)–(11) for  $N = 2$ .

It is then a standard exercise to show that the extremal values of the longitudinal magnetization in the state, which is an arbitrary superposition of  $|GS_+\rangle$  and  $|GS_-\rangle,$  are

$$\begin{aligned} M_x &= \pm\langle GS_-|\sigma_i^x|GS_+\rangle = \pm M_x^{\text{eq}} \\ &= \pm\frac{1}{2}\left(\sqrt{1+\frac{g}{\sqrt{1+g^2}}} + \sqrt{1-\frac{g}{\sqrt{1+g^2}}}\right). \end{aligned} \tag{26}$$

This formula is depicted in figure 1, where one easily notices its departures from thermodynamic limit expression (7). These differences do not vanish in the whole paramagnetic phase. In fact, for a periodic system composed of  $N$  spins, it is easy to show that the longitudinal magnetization does not vanish in the limit of  $g \rightarrow \infty$

$$M_x^{\text{eq}}(g \rightarrow \infty) = \frac{1}{\sqrt{N}}. \tag{27}$$

Such a simple result follows from elementary observation that in the limit of  $g \rightarrow \infty$  the positive parity ground state approaches  $|\uparrow\uparrow\uparrow\cdots\rangle,$  while the negative parity one approaches

$$\frac{|\downarrow\uparrow\uparrow\cdots\rangle + |\uparrow\downarrow\uparrow\cdots\rangle + |\uparrow\uparrow\downarrow\cdots\rangle + \cdots}{\sqrt{N}}. \tag{28}$$

#### 4. Dynamics of periodic chains

We will discuss here dynamics of the longitudinal magnetization in a periodic Ising chain. There are different ways how one can approach this problem.

The most direct one is to work in the Fock space spanned by all combinations of up/down states of all spins such as  $|\uparrow\downarrow\uparrow\cdots\rangle$ . Such a space can be then easily cut into positive and negative parity subspaces, where time evolutions can be independently performed. The advantage of such an approach is that it allows for easy computation of the longitudinal magnetization. The disadvantage is rather obvious: one has to keep track of  $2 \times 2^{N-1}$  amplitudes, which highly limits the available system sizes.

Another approach relies on mapping the system onto non-interacting fermions via the Jordan–Wigner transformation (A.1). This reduces the problem to finding time-evolution of  $N - 1$  two-level uncoupled systems (A.8), which can be straightforwardly numerically achieved. This is the most efficient way of getting wave-function (14). The problem with this approach, however, lies in the complexity of the computation of the longitudinal magnetization, which we explain in appendix A.

We will thus use the first above-mentioned approach, i.e. the direct numerical solution, to characterize dynamics of the  $N = 12$  periodic chain. In the next section, we will sacrifice the translational invariance by doing calculations in much larger chains with open boundaries, where such problems with computation of the longitudinal magnetization are absent.

The results of our numerical simulations, starting from initial state (3) and employing quench protocol (4), are presented in figures 3–5, where we have chosen quench time  $\tau_Q$  large-enough to ensure that evolutions will be nearly adiabatic. We see there that after stopping the driving, say for

$$0 \leq t \leq L, \quad (29)$$

there are periodic oscillations, which will be studied in various ways.

First, we will extract from numerical data the difference between positions of the first two maxima of  $M_x(t)$  and use it to compute the frequency  $\omega_{12}$  of oscillations. We will also get from such data half of the difference between  $M_x(t)$  in the first maximum and the second minimum to obtain the oscillation amplitude  $A_{12}$ . These quantities are illustrated in figure 3. The frequency  $\omega_{12}$  and amplitude  $A_{12}$  estimate  $\delta(g_f)$  and  $M_x^{\text{eq}}(g_f)$  –see (17) for justification of this statement<sup>1</sup>. As far as numerical simulations are concerned, the uncertainty of getting  $\omega_{12}$  and  $A_{12}$  is negligible. This is perhaps the easiest way of characterization of after-quench oscillations as it requires observation of no more than two oscillation periods.

Second, we will fit the periodic function

$$M_x(t) = A_{\text{fit}} \cos(\omega_{\text{fit}} t + \text{const}) \quad (30)$$

expecting that  $\omega_{\text{fit}}$  and  $A_{\text{fit}}$  will estimate the same physical quantities as  $\omega_{12}$  and  $A_{12}$ . Such fitting will be done with NonlinearModelFit function from [35]. This function also provides uncertainty of the fitted parameters, which is negligible in our studies of  $\omega_{\text{fit}}$  and  $A_{\text{fit}}$ . A few oscillation periods provide enough data for reaching the full potential of this technique.

<sup>1</sup> Note that we work with  $\hbar = 1$ , where the frequency and the energy can be directly compared.

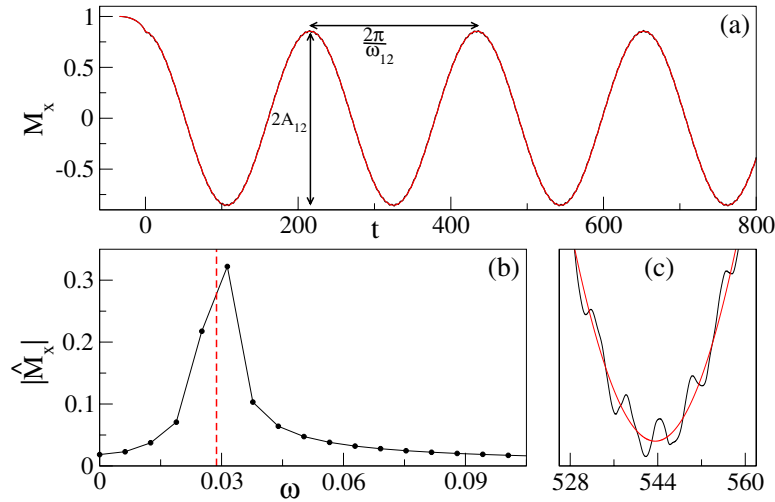


**Figure 3.** Dynamics of the longitudinal magnetization in a periodic system for a nearly adiabatic quench that stops in the ferromagnetic phase at  $g_f = 0.85$ . The driving ends at the time  $t = 0$  and then free evolution begins. Panel (a): the black line shows numerics, while the red one shows adiabatic approximation (16). Panel (b): modulus of the discrete Fourier transform (31) of free evolution of the longitudinal magnetization around the symmetry-breaking gap  $\delta$  marked by the vertical red dashed line. Data points are joined by line segments to guide the eye. Panel (c): magnification of the area around the third minimum from panel (a). The system size is  $N = 12$ , the quench time is  $\tau_Q = 40$ , and the time span of free oscillations used for computing (31) is  $L = 1000$ .

Third, we will compute the discrete Fourier transform

$$\hat{M}_x(\omega_j) = \frac{1}{S} \sum_{s=0}^{S-1} M_x(s\Delta t) e^{i\omega_j s\Delta t}, \quad (31)$$

$$\Delta t = \frac{L}{S}, \quad \omega_j = \frac{2\pi j}{L}, \quad j = 0, 1, \dots, S-1,$$

where  $S$  is the number of data points that we generate during free evolution. We will work with  $S$  being of the order of a few tens of thousands (its exact value is of marginal use in the following discussion). We will look for the global maximum of  $|\hat{M}_x|$  studying its position  $\omega_{\max}$  and value  $|\hat{M}_x(\omega_{\max})|$ . The former will estimate  $\delta$ . The latter, after multiplication by a factor of two, will be of the order of  $M_x^{\text{eq}}$ . We will thus introduce  $A_{\max} = 2|\hat{M}_x(\omega_{\max})|$  in analogy to the notation that we have used above. Both remarks follow from (17) and (31).

We have applied all these techniques to numerics from figures 3(a)–5(a) getting results that are presented in table 2. We see there very good agreement between the oscillation frequencies  $\omega_{12}$  and  $\omega_{\text{fit}}$  and the values of the symmetry-breaking gap  $\delta$  from table 1. Moreover, similar agreement is found between the oscillation amplitudes  $A_{12}$  and  $A_{\text{fit}}$  listed in table 2 and  $M_x^{\text{eq}}$  from table 1.

If we, however, use data from these tables to compare  $\omega_{\max}$  and  $A_{\max}$  to the symmetry-breaking gap and the equilibrium longitudinal magnetization, we will find much

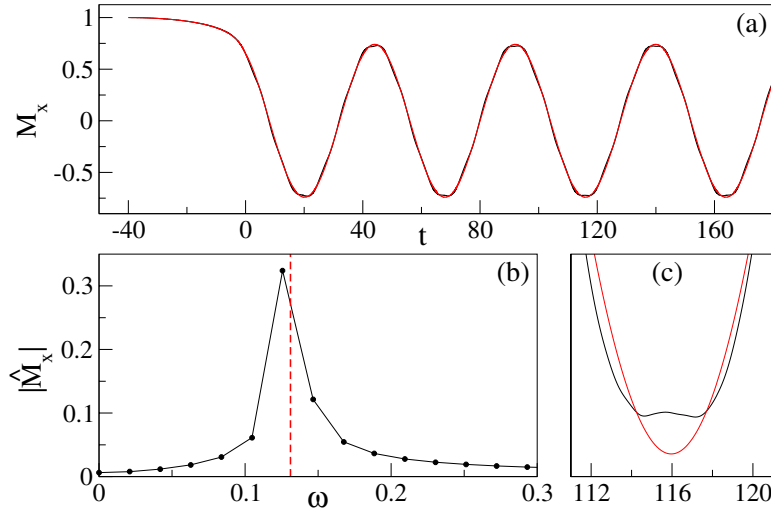


**Figure 4.** Dynamics of the longitudinal magnetization in a periodic system for a nearly adiabatic quench that stops at the critical point. This figure is organized in the same way as figure 3. The parameters are  $g_f = 1$ ,  $N = 12$ ,  $\tau_Q = 40$ , and  $L = 300$ .

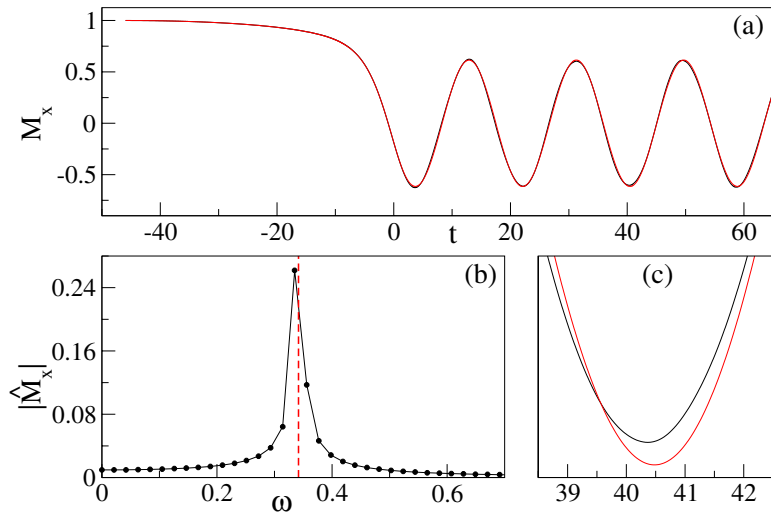


**Figure 5.** Dynamics of the longitudinal magnetization in a periodic system for a nearly adiabatic quench that stops in the paramagnetic phase. This figure is organized in the same way as figure 3. The parameters are  $g_f = 1.15$ ,  $N = 12$ ,  $\tau_Q = 40$ , and  $L = 300$ .

larger relative discrepancies. Estimation of the symmetry-breaking gap through  $\omega_{\max}$  is mostly affected by the spectral resolution of the Fourier transform

$$2\pi/L. \tag{32}$$

This is seen in figures 3(b)–5(b), where the horizontal spacing between the data points ranges between 0.006 and 0.02, which is non-negligible relative to  $\delta$ . Estimation of the equilibrium longitudinal magnetization through  $A_{\max}$  is additionally influenced by population of different Fourier modes decreasing  $|\hat{M}(\omega_{\max})|$  with respect to its adiabatic

**Table 2.** Parameters describing free oscillations of the longitudinal magnetization from figures 3–5 (top to bottom). Symbols  $\omega_{12}$ ,  $\omega_{\text{fit}}, \dots$ ,  $A_{\text{max}}$  are defined around equations (30) and (31). The fitting leading to  $\omega_{\text{fit}}$  and  $A_{\text{fit}}$  has been done on time intervals  $0 \leq t \leq 4 \times 2\pi/\delta(g_f)$  corresponding to four oscillation periods during free evolution.

	$\omega_{12}$	$\omega_{\text{fit}}$	$\omega_{\text{max}}$	$A_{12}$	$A_{\text{fit}}$	$A_{\text{max}}$
$g_f = 0.85$	0.028 422	0.028 747	0.031 416	0.8620	0.8538	0.64
$g_f = 1$	0.131 14	0.131 08	0.125 66	0.7286	0.7397	0.65
$g_f = 1.15$	0.341 77	0.341 74	0.335 10	0.6178	0.6146	0.52

value. This can be seen through Plancherel theorem. Finally, mismatch between the symmetry-breaking gap and the frequency grid  $\{\omega_j\}$  additionally affects  $|\hat{M}(\omega_{\text{max}})|$ .

A good agreement that we have found using the first two approaches is the result of choosing so large quench time  $\tau_Q$ , that evolutions are nearly adiabatic. If we now take a look at figures 3(c)–5(c), we will be able to notice small deviations from perfectly adiabatic solution (16). Similar features will be seen in the simulations of chains with open boundaries, which brings us to the next section of this work, where they will be discussed.

## 5. Dynamics of chains with open boundaries

We will study in this section dynamics of Ising chains with open boundaries. Such systems are described by the following Hamiltonian

$$\tilde{H}(g) = - \sum_{i=1}^{N-1} \sigma_i^x \sigma_{i+1}^x - \sum_{i=1}^N g \sigma_i^z. \quad (33)$$

There are at least two reasons for their consideration.

First, they are more experimentally-relevant than the periodic chains as it is a very complicated task to engineer a periodic coupling between the spins (see e.g. [36] for an elaborate proposal how this might be achieved in a cold ion simulator of spin systems).

Second, computations of the longitudinal magnetization can be efficiently done in the chains with open boundaries. It is so because the parity operator (8) does not appear during the diagonalization of Hamiltonian (33) and so both parity subspaces are diagonalized with one and the same set of transformations (see appendix A for explanation why this is not the case in periodic chains and note that  $\tilde{H}$  commutes with the parity operator). This allows for efficient evaluation of the longitudinal magnetization in systems composed of up to a few hundreds of spins, which is a major step forward with respect to our studies of periodic chains. This flexibility with respect to the system size allows us for systematic studies of the transition from the non-equilibrium regime, where the Kibble–Zurek theory describes the system’s excitation, to the nearly adiabatic regime, which we have already begun to investigate in section 4.

Moving on to the actual calculations, we mention that technical details related to diagonalization of Hamiltonian (33) and time evolution that it generates are presented in appendix B. We only summarize here some basic formulae that are necessary for understanding of the following discussion.

After Jordan–Wigner mapping (A.1), the Hamiltonian is diagonalized by the Bogolubov transformation so that it finally reads

$$\tilde{H} = \sum_{i=1}^N E_i \left( \gamma_i^\dagger \gamma_i - 1/2 \right), \tag{34}$$

$$\{\gamma_i, \gamma_j^\dagger\} = \delta_{ij}, \quad \{\gamma_i, \gamma_j\} = 0,$$

where the energies of single-particle excitations, defined in our work with respect to the ground state energy, are sorted in ascending order,  $E_1 \leq E_2 \leq \dots \leq E_N$ , so that the symmetry-breaking gap is

$$\delta = E_1. \tag{35}$$

They are given by

$$E_i = 2\sqrt{g^2 - 2g \cos \theta_i + 1}, \tag{36}$$

where  $\theta_i$ 's are obtained from [37]

$$g \sin[(N + 1)\theta] = \sin(N\theta), \quad 0 < \theta < \pi. \tag{37}$$

For  $g > N/(N + 1)$ ,  $\theta_1, \dots, \theta_N$  are the real roots of (37). For  $0 \leq g \leq N/(N + 1)$ , most interestingly, there is one purely imaginary solution of (37),  $\text{Re}(\theta_1) = 0$ . Besides that, there are  $N - 1$  real roots of (37):  $\theta_2, \dots, \theta_N$ . Equation (37) cannot be solved analytically for an arbitrary value of the magnetic field  $g$ . Its numerical solutions, relevant for the subsequent discussion, are collected in table 3.

Besides the symmetry-breaking gap, we are also interested in the longitudinal magnetization, which is now position dependent. Its equilibrium value in the Ising chain with open boundaries was recently discussed in [38], where it was analyzed how the ‘ends’ of the chain affect its value. To minimize their influence on our results, we will focus our attention on the center of the system by calculating

$$M_x = \langle \sigma_{N/2}^x \rangle. \tag{38}$$

The equilibrium values of such defined longitudinal magnetization, for the parameters relevant for the subsequent discussion, are listed in table 4. The technical details of computation of (38) are discussed in appendix B.

An important thing now is to note that if we write the Schrödinger-picture wavefunction at the time the quench stops as

$$|\psi(t = 0)\rangle = \sum_{i_1 i_2 \dots i_N} a_{i_1 i_2 \dots i_N} |i_1 i_2 \dots i_N\rangle, \tag{39}$$

$$\sum_{i_1 i_2 \dots i_N} |a_{i_1 i_2 \dots i_N}|^2 = 1,$$

**Table 3.** Energies of single-particle excitations relevant for deciphering the positions of marked maxima in figures 6, 7 and 9.

	$E_1$	$E_2$	$E_3$	$E_4$	$E_5$	$E_6$	$E_7$
$g_f = 0.85, N = 20$	0.0217	0.470	0.730				
$g_f = 1, N = 50$	0.0622	0.187	0.311	0.435	0.558	0.681	0.803
$g_f = 1.15, N = 50$	0.322	0.383	0.470				

**Table 4.** The equilibrium longitudinal magnetization in the Ising chain with open boundaries for the parameters relevant to the studies reported in figures 6–8.

	$M_x^{\text{eq}}$
$g = 0.85, N = 20$	0.8448
$g = 1, N = 50$	0.6188
$g = 1.15, N = 50$	0.4204

$$|i_1 i_2 \dots i_N\rangle = \left(\gamma_1^\dagger\right)^{i_1} \left(\gamma_2^\dagger\right)^{i_2} \dots \left(\gamma_N^\dagger\right)^{i_N} |GS\rangle,$$

$$i_n = 0, 1 \text{ and } \gamma_n |GS\rangle = 0 \text{ for } 1 \leq n \leq N,$$

then at times  $t > 0$

$$M_x(t) = \sum_{\substack{j_1 j_2 \dots j_N \\ i_1 i_2 \dots i_N}} \overline{a_{j_1 j_2 \dots j_N}} a_{i_1 i_2 \dots i_N} e^{it \sum_{n=1}^N (j_n - i_n) E_n} \langle j_1 j_2 \dots j_N | \sigma_{N/2}^x | i_1 i_2 \dots i_N \rangle \quad (40)$$

with

$$\sum_{n=1}^N (i_n + j_n) \text{ being odd.} \quad (41)$$

If this condition is not satisfied, then the matrix element in (40) identically vanishes, which can be shown with Wick’s theorem. This feature impacts Fourier spectra of the longitudinal magnetization.

### 5.1. Quenches stopping in ferromagnetic or paramagnetic phase

We start discussion of our numerical simulations from the non-equilibrium quench that has been stopped in the ferromagnetic phase (figure 6). The first thing that catches our attention in this figure is ‘roughness’ of free evolution of  $M_x$ . To understand it, we need to look at modulus of its discrete Fourier transform.

By doing so, we first notice a series of peaks enumerated by  $A, B$ , etc whose maxima are placed at  $\omega_A, \omega_B$ , etc listed in table 5. If we now use data from table 3 and equations (40) and (41), we can note that within spectral resolution of the Fourier transform  $\omega_A, \omega_B, \omega_C$ , and  $\omega_D$  can be identified with  $E_1, E_3 - E_1 - E_2, E_2$ , and  $E_3$ , respectively.

Occupation of the Fourier modes around  $\omega_A$  is responsible for the oscillation period  $2\pi/\delta(g_f)$  marked in the upper panel of figure 6. Next, we note that (i)  $\omega_B, \omega_C$ , etc are

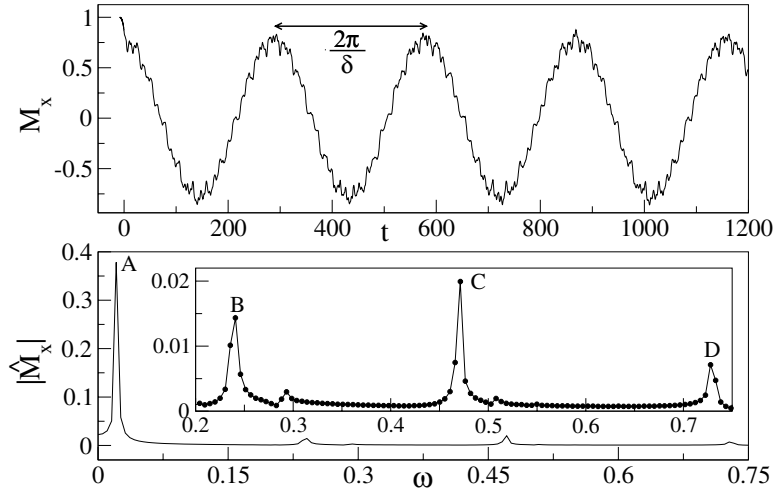


**Figure 6.** Upper panel: dynamics of the longitudinal magnetization in the Ising chain with open boundaries for the quench that stops in the ferromagnetic phase. The parameters are  $g_f = 0.85$ ,  $N = 20$ , and  $\tau_Q = 10$ .  $\delta$  is given by  $E_1$  from table 3 (first row). Lower panel: modulus of the discrete Fourier transform of free evolution data, i.e.  $M_x(t > 0)$ , from the upper panel. The inset enlarges peaks B–D.  $L = 1200$  has been used to compute the transform.

larger by at least a factor of ten than  $\omega_A$  and (ii)  $|\hat{M}_x(\omega_A)|$  is larger by at least a factor of fifteen than  $|\hat{M}_x(\omega_B)|$ ,  $|\hat{M}_x(\omega_C)|$ , etc. The (i) observation means that there will be high frequency oscillations on top of the base oscillation, whose frequency is approximated by  $\omega_A$ . The (ii) remark implies that they will have small amplitude relative to the amplitude of the base oscillation. Both features are nicely seen in the upper panel of figure 6. They explain small fluctuations of the data presented there.

A quite different situation is encountered when the quench stops in the paramagnetic phase. This is illustrated in figure 7, where we see beats. A simple explanation of this observation comes again from the discrete Fourier transform, where we see two leading peaks centered around  $\omega_A$  and  $\omega_B$ . The beats result from the fact that  $|\hat{M}_x(\omega_A)|$  is comparable to  $|\hat{M}_x(\omega_B)|$ . Moreover, we note that  $\omega_A$ ,  $\omega_B$ , and  $\omega_C$  are of the same order of magnitude, which eliminates high frequency oscillations seen in figure 6. Looking more quantitatively at the Fourier transform from figure 7, we notice that  $\omega_A$ ,  $\omega_B$ , and  $\omega_C$  can be identified with  $E_1$ ,  $E_2$ , and  $E_3$  within the spectral resolution of the Fourier transform (tables 3 and 5).

Finally, at the risk of stating the obvious, we mention that we recover adiabatic results, akin to those presented in figures 3 and 5, by increasing the quench times from figures 6 and 7. In the opposite limit of fast transitions, free evolution of the longitudinal magnetization becomes noisy and so less interesting in the context of our studies.

## 5.2. Quenches to critical point

We will discuss now the transition to the adiabatic regime for evolutions ending at the critical point. Such evolutions are depicted in figure 8. For small  $\tau_Q$ , we see a train of narrow peaks, whose amplitude decreases as time goes by. The magnetization in

**Table 5.** The positions of maxima of  $|\hat{M}_x|$  marked in figures 6, 7 and 9.

	$\omega_A$	$\omega_B$	$\omega_C$	$\omega_D$	$\omega_E$	$\omega_F$	$\omega_G$
$g_f = 0.85, N = 20$	0.0209	0.241	0.471	0.728			
$g_f = 1, N = 50$	0.0628	0.188	0.308	0.434	0.559	0.685	0.804
$g_f = 1.15, N = 50$	0.325	0.382	0.471				

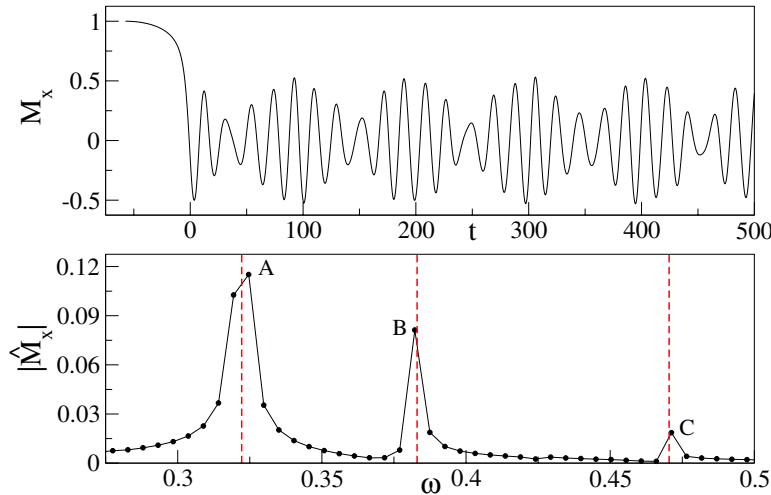


**Figure 7.** Upper panel: dynamics of the longitudinal magnetization in the Ising chain with open boundaries for the quench that stops in the paramagnetic phase. The parameters are  $g_f = 1.15$ ,  $N = 50$ , and  $\tau_Q = 50$ . Lower panel: modulus of the discrete Fourier transform of the free evolution data from the the upper panel. The vertical red dashed lines in the lower panel show energies of the single-particle excitations from the third row of table 3.  $L = 1200$  has been used to compute the transform.

between the peaks is nearly zero. As evolutions slow down, the decay of the peaks' amplitude slows and the peaks' width increases shrinking time intervals, where the system is unmagnetized in the longitudinal direction. By the time those intervals disappear, the curve describing dynamics of the longitudinal magnetization has a triangular-like shape. Further increase of the quench time brings the expected single-frequency dynamics characteristic of the adiabatic evolution (17).

The rather unusual shape of oscillations of the longitudinal magnetization for the fastest quenches from figure 8 comes from substantial population of several Fourier modes. This is illustrated in figure 9, where the subsequent Fourier peaks are centered at the energies of consecutive single-particle excitations (tables 3 and 5).

The question now is why the period of these oscillations is approximately given by  $2\pi/\delta(g = 1)$ . This would be an expected result for adiabatic evolutions, where the oscillation pattern would be cosinusoidal (17). It may thus be a bit surprising that multi-frequency oscillations from figure 8 exhibit the same period. This can be understood by noting that

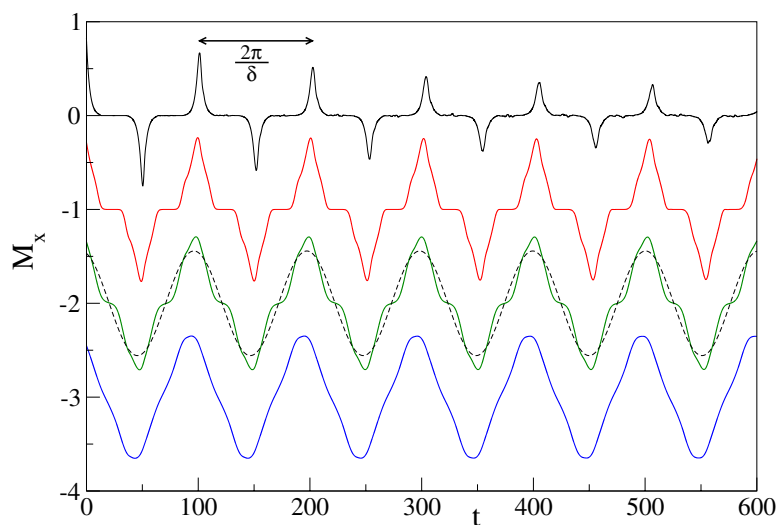


**Figure 8.** Free evolution of the longitudinal magnetization after quenches to the critical point in the Ising chain with open boundaries. The solid curves, from top to bottom, correspond to  $\tau_Q = 2$  (black),  $\tau_Q = 20$  (red),  $\tau_Q = 73$  (green), and  $\tau_Q = 200$  (blue). The subsequent curves are shifted downward by a multiple of 1 to facilitate their comparison. The dashed black curve shows  $0.557 \cos(0.0622t + 0.307)$  shifted downward by 2. It comes from the fit to the numerics for  $\tau_Q = 73$ , which is close to the crossover quench time discussed in figure 10. The parameters are  $g_f = 1$  and  $N = 50$ .  $\delta$  is given by  $E_1$  from table 3 (second row).

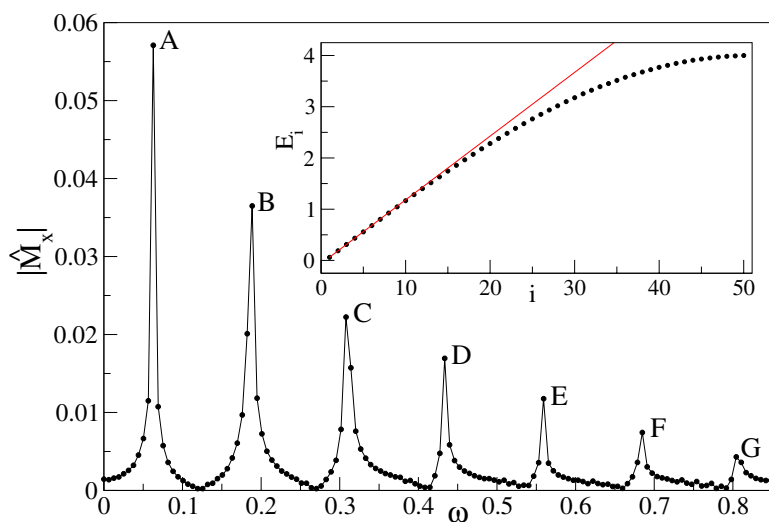


**Figure 9.** Modulus of the discrete Fourier transform of free evolution of the longitudinal magnetization of the fastest quench from figure 8:  $g_f = 1$ ,  $N = 50$ ,  $\tau_Q = 2$ .  $L = 1000$  is used to compute the transform. The inset shows (36) for  $g = 1$  and  $N = 50$ . The black dots in the inset are obtained from numerical solution of (37), while the solid red line shows (42) with  $\delta(g = 1)$  given exactly by (B.4).

$$E_i \approx (2i - 1)\delta(g = 1) \approx (2i - 1)\frac{\pi}{N} \quad (42)$$

for the lowest-energy modes—see the second row of table 3, (B.4), and the inset of figure 9. If such a relation would hold for all  $E_i$ 's, then the oscillations of the longitudinal magnetization during free evolution would be perfectly adiabatic with the  $2N$  period regardless of the quench time  $\tau_Q$ . Relation (42), however, is approximate, which we also illustrate in the inset of figure 9. This explains quasi-periodicity of the oscillation pattern for the fastest quench in figure 8. For a bit slower, but still non-adiabatic quenches depicted in this figure, (42) properly captures these single-particle excitation energies that give the main contribution to the free dynamics of  $M_x(t)$ . This is sufficient for explanation of the oscillation period from figure 8.

This oscillation period is twice smaller than the oscillation period at the critical point of the periodic system, which can be trivially shown with (11). The linear dependence of the oscillation period on the system size, albeit with a different prefactor, was also observed in our earlier studies of the quantum Ising model [20], where we investigated free dynamics of the transverse magnetization after quenches moving the system from the paramagnetic phase to the critical point. Finally, we mention that approximation (42) works only at the critical point, which explains why different dynamics have been observed in section 5.1.

To study quantitatively the crossover from the non-equilibrium to the adiabatic regime, which we depict in figure 8, we need some measure of the deviation of non-equilibrium evolution from the adiabatic limit. A good measure should be easily numerically and experimentally accessible. It should be also stable against fluctuations of the data for  $M_x(t)$ . Several options seem to be available.

First, one may analyze modulus of the discrete Fourier transform. For example, one can study how the global maximum around the symmetry-breaking gap grows with increasing  $\tau_Q$ . Alternatively, one may research how the other extrema disappear in such a limit. This choice, however, is problematic for the reasons explained by the end of section 4. For example, there are limitations imposed by the spectral resolution of the discrete Fourier transform (32). To overcome them, either long free evolution times are needed or some fitting procedure allowing for precise interpolation of the properties of extrema of  $|\hat{M}_x|$  from sparse data. This is a complication affecting both numerical and experimental studies. The latter would be also affected by the fact that the Fourier transform is not directly measured and so its extraction out of  $M_x(t)$  will necessarily bring some inaccuracies that may play a role in the Kibble–Zurek scaling analysis.

Second, one may use a more straightforward approach by studying the amplitude and spacing of the first two peaks of  $M_x(t)$ , just as in section 4. Such a method, however, is susceptible to fluctuations of the data. This can be improved by averaging results collected for several peaks, but this would again require long free evolution times, which is problematic.

Third, one may fit (30) to free evolution of the longitudinal magnetization and study such obtained amplitude of oscillations  $A_{\text{fit}}$  (figure 10). Such a procedure uses all information contained in  $M_x(t)$ —not only the one stored in the extrema of either  $M_x$  or  $|\hat{M}_x|$ —and so long evolution times are not needed. Moreover, it should work well with irregular data averaging out the fluctuations, which is of interest in the context of

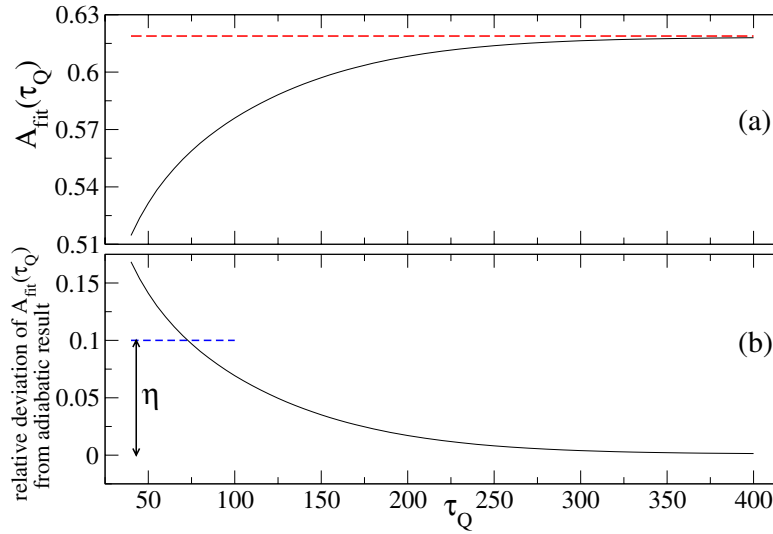


**Figure 10.** Panel (a): the fitted amplitude of oscillations of the longitudinal magnetization after stopping the quench at the critical point of the Ising chain with open boundaries. The solid black line shows numerics in both panels. The dashed red line shows the result for perfectly adiabatic evolution to the critical point, which is given by the equilibrium magnetization (second row of table 4). Panel (b): the left-hand side of (43). The dashed blue line shows the threshold  $\eta = 10\%$  from (43). Its intersection with the solid black line gives  $\tau_Q^{\text{cross}} \approx 72.83$ . The system size is  $N = 50$ .

high-precision numerical and experimental research. This is the approach that we will employ.

Before moving on, we again mention that the fitted amplitude  $A_{\text{fit}}$  converges to  $M_x^{\text{eq}}(g_f)$  in the adiabatic limit. For faster quenches, however, it underestimates the real amplitude of oscillations, which is seen in figure 8. This has no effect on our studies, which is perhaps best illustrated by the excellent agreement between the scaling exponent extracted out of the fitted amplitude and the predictions of the Kibble–Zurek theory (see below).

To proceed, we define the crossover quench time  $\tau_Q^{\text{cross}}$  by the condition

$$\left| \frac{A_{\text{fit}}(\tau_Q) - M_x^{\text{eq}}(g_f)}{M_x^{\text{eq}}(g_f)} \right| < \eta \quad \text{for } \tau_Q > \tau_Q^{\text{cross}}, \quad (43)$$

where  $\eta$  is the threshold set on the relative difference between the fitted amplitude of oscillations and its asymptotic in  $\tau_Q$  value. We will use in this formula the amplitude obtained by fitting (30) to  $M_x(t)$  for  $0 \leq t \leq 12N$ , which corresponds to roughly 6 oscillation periods in the chain with open boundaries. Moreover, we will set  $\eta = 10\%$ , which should be large-enough to be experimentally-relevant and small-enough to describe the crossover to the adiabatic limit.

Our results for  $A_{\text{fit}}$ , in the experimentally-relevant system composed of  $N = 50$  spins [39–41], are presented in figure 10(a), where we see that the fitting procedure produces a perfectly smooth curve monotonically approaching  $M_x^{\text{eq}}(g_f)$ . The threshold  $\eta$  is illustrated in figure 10(b).

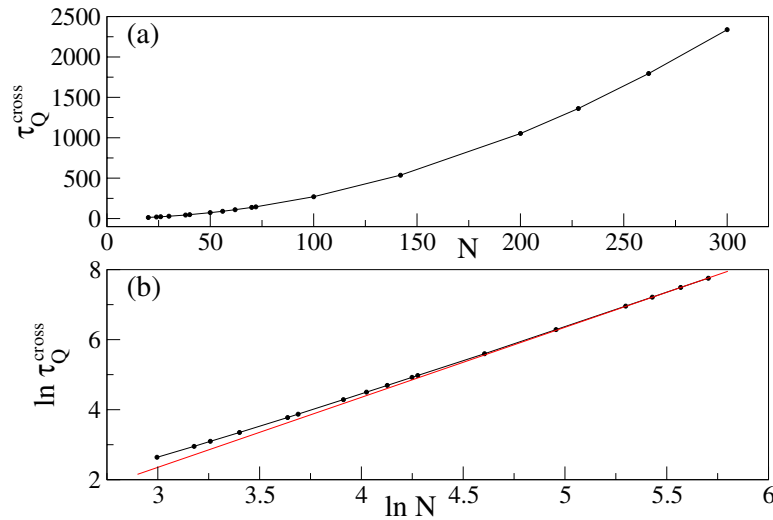


**Figure 11.** Panel (a): the crossover quench time  $\tau_Q^{\text{cross}}$  as a function of the system size for quenches that stop at the critical point of the Ising chain with open boundaries ( $g_f = 1$ ). Dots come from numerics, line segments join them to guide the eye. The threshold from (43) is  $\eta = 10\%$ . Panel (b): data from the upper panel shown on a double logarithmic plot. The solid red line has the slope equal to +2 and the intercept fitted to the two largest- $\tau_Q$  data points.

**Table 6.** The results of fitting (45) to numerical data in different ranges of the system sizes (either four or five data points are used for each linear regression). We provide one standard error in the brackets delivered by the LinearModelFit function from [35].

	$a$	$b$
$20 \leq N \leq 30$	1.75(1)	-2.60(4)
$38 \leq N \leq 62$	1.871(3)	-3.03(1)
$70 \leq N \leq 142$	1.92(1)	-3.26(6)
$200 \leq N \leq 300$	1.970(4)	-3.48(2)

Repeating such analysis for system sizes  $20 \leq N \leq 300$ , we have obtained detailed results for the crossover quench time  $\tau_Q^{\text{cross}}$ , which we present in figure 11(a). As we anticipate from (19) that

$$\tau_Q^{\text{cross}}(N) \sim N^a, \quad (44)$$

where  $a > 0$  is the scaling exponent, we display results for  $\tau_Q^{\text{cross}}$  on a double logarithmic plot in figure 11(b). Instead of a straight line, we find in this figure a curve slightly bending upwards as the system size grows. This means that the exponent  $a$  increases with  $N$ . To quantify this observation, we fit

$$\ln \tau_Q^{\text{cross}} = a \ln N + b \quad (45)$$

to numerical data from four different ranges of the system sizes. The results are collected in table 6, where we see that  $a$  approaches the value of 2 for the largest system sizes that we consider. This is in a very good agreement with the Kibble–Zurek scaling argument (19), which is supposed to work best in the large-system limit. Finally, we

notice that the increase of  $a$  with  $N$  is monotonic, leaving no doubts about stability of the procedure of extraction of  $\tau_Q^{\text{cross}}$  from the free evolution data for the longitudinal magnetization.

## 6. Discussion

The goal of this work was to investigate how the symmetry-breaking gap, which is of crucial importance in the discussion of quantum phase transitions, can be studied with the help of quantum quenches. We have chosen for this purpose an exactly solvable model, the quantum Ising model in the transverse field, and analyzed its dynamics after quenches induced by the gradual change of the magnetic field. These quenches start from the easy-to-prepare broken-symmetry ground state at the vanishing magnetic field. They bring the system to the desired value of this field, where the symmetry-breaking gap can be read from the subsequent free-evolution dynamics of the longitudinal magnetization. In this way a small symmetry-breaking gap can be seen through large-amplitude oscillations of the longitudinal magnetization.

We have discussed different ways of analyzing the oscillatory dynamics of such magnetization showing that one can also extract the equilibrium longitudinal magnetization out of them. All this can be accurately done if the quench is slow enough, which we have studied in the context of the Kibble–Zurek theory of non-equilibrium phase transitions. An excellent agreement between predictions of this theory and the dynamics of the longitudinal magnetization has been found.

Although our studies have been done in the Ising model, they can be extended to other systems exhibiting the symmetry-breaking phenomenon. For example, the Ising-like ones with long-range interactions that are typically found in cold ion and atom emulators of spin systems (see e.g. [4, 23, 36, 42, 43]). These systems provide a promising platform for experimental realization of the studies discussed in our work for two reasons. First, their size is finite rather than thermodynamic making their symmetry-breaking gap large-enough to be experimentally measurable. This should not be taken for granted because it is not the case in traditional condensed matter setups discussed in the context of phase transitions. Second, there has been substantial progress in the experimental studies of the dynamics of such systems (see e.g. [39–41]).

Another promising platform for implementation of our ideas is provided by D-Wave machines, which can be also used for simulations of spin models (see e.g. [44]). Quite interestingly, D-Wave-based investigations of non-equilibrium Kibble–Zurek dynamics of the one-dimensional quantum Ising model in the transverse field were recently reported in [45]. It should be thus possible to use our predictions for critical assessment of the performance of such devices.

Talking about experimental realizations, the symmetry-breaking phenomenon was recently experimentally investigated in [24]. These studies were done in a cold atom cloud, where each atom was simulating the 16-spin Lipkin–Meshkov–Glick model. This is the Ising-like model with the nearest-neighbor spin–spin interactions replaced with identical couplings between all the spins. Besides exploration of a different Hamiltonian, these interesting studies differ from our work in the following aspects. First, the quenches

start in the paramagnetic phase. Second, the initial state for them occupies one of the parity subspaces and so the symmetry-breaking perturbation is used to populate the other one as well. Third, perhaps most importantly, they are limited to one, rather small system size, and they do not explore the non-adiabatic Kibble–Zurek dynamics of the longitudinal magnetization, which is of considerable importance in our work.

Finally, we mention that we hope that this work will trigger interest in the experimental studies of the symmetry-breaking phenomenon, which could lead to quantitative insights into the very nature of quantum phase transitions. This would be most interesting in systems that can be neither analytically nor numerically studied in the foreseeable future.

### Acknowledgments

We thank Marek Rams for useful discussions, sharing with us the results of his numerical simulations, reading the manuscript, and providing us with most useful feedback. MB and BD were supported by the Polish National Science Centre (NCN) Grant DEC-2016/23/B/ST3/01152.

### Appendix A. Longitudinal magnetization in Jordan–Wigner-transformed periodic Ising chains

We will explain here the source of difficulties in computation of the longitudinal magnetization in the free fermion representation of the periodic Ising model. While doing so, we will also derive expressions for dynamical gaps  $\Delta_{\pm}$ , which have been introduced in section 2.

Such a representation comes from employment of the Jordan–Wigner transformation

$$\sigma_i^z = 1 - 2c_i^\dagger c_i, \quad \sigma_i^x = (c_i + c_i^\dagger) \prod_{j<i} (1 - 2c_j^\dagger c_j),$$

$$\{c_i, c_j^\dagger\} = \delta_{ij}, \quad \{c_i, c_j\} = 0,$$
(A.1)

after which Hamiltonian (1) reads

$$H(g) = - \sum_{i=1}^{N-1} f_{i,i+1} - g \sum_{i=1}^N (c_i c_i^\dagger - c_i^\dagger c_i) + f_{N,1} P, \quad f_{i,j} = c_i^\dagger c_j - c_i c_j^\dagger - c_i c_j + c_i^\dagger c_j^\dagger.$$
(A.2)

The complication one encounters now is that the parity operator is not quadratic in fermionic  $c_i$  and  $c_i^\dagger$  operators. This can be found by combining (8) with (A.1). As a result, Hamiltonian (A.2) is non-quadratic. Its exact analytical diagonalization is still possible, but the price one has to pay is that one has to split the Hilbert space into positive and negative parity subspaces imposing different boundary conditions on the fermionic operators in those subspaces [28]. This is realized by going to the momentum space

$$c_j = \frac{e^{-i\pi/4}}{\sqrt{N}} \sum_k c_k e^{ikj}, \tag{A.3}$$

and choosing different quantization schemes for momenta in the positive and negative parity subspaces,

$$k_+ = \pm \frac{\pi}{N}, \pm \frac{3\pi}{N}, \dots, \pm \frac{N-1}{N} \pi, \tag{A.4}$$

and

$$k_- = 0, \pm \frac{2\pi}{N}, \pm \frac{4\pi}{N}, \dots, \pm \frac{N-2}{N} \pi, \pi, \tag{A.5}$$

respectively. These expressions are valid for even  $N$  (see [28] for comprehensive discussion of the Ising diagonalization intricacies). Therefore, different transformations are used to diagonalize the two parity subspaces in periodic chains. No such complications appear in the chains with open boundaries, where the parity operator is absent in Jordan-Wigner-transformed Hamiltonian (B.1).

Combining the results of [5] and [28], time-dependent wave-function (14) can be obtained from

$$|\psi_+(t)\rangle = \prod_{k_+ > 0} \left( u_{k_+}(t) - v_{k_+}(t) c_{k_+}^\dagger c_{-k_+}^\dagger \right) |\text{vac}\rangle, \tag{A.6}$$

$$|\psi_-(t)\rangle = e^{2it} c_0^\dagger \prod_{0 < k_- < \pi} \left( u_{k_-}(t) - v_{k_-}(t) c_{k_-}^\dagger c_{-k_-}^\dagger \right) |\text{vac}\rangle, \tag{A.7}$$

where the state  $|\text{vac}\rangle$  is annihilated by all  $c_k$  operators and time evolution of the Bogolubov modes is governed by

$$i \frac{d}{dt} \begin{pmatrix} v_k \\ u_k \end{pmatrix} = 2 \begin{pmatrix} g - \cos(k) & -\sin(k) \\ -\sin(k) & \cos(k) - g \end{pmatrix} \begin{pmatrix} v_k \\ u_k \end{pmatrix}. \tag{A.8}$$

Computation of the time-dependent longitudinal magnetization in our periodic system is now reduced to evaluation of

$$M_x(t) = \langle \psi_-(t) | c_1 + c_1^\dagger | \psi_+(t) \rangle + \text{c.c.} \tag{A.9}$$

If we now put (A.6) and (A.7) into (A.9) and then transform  $c_{k_\pm}$  operators to the position space inverting (A.3)—so that all operators are defined on the same Hilbert space—we will quickly realize how complicated the resulting expression is. This obstacle discourages us from using the free fermion representation in our studies of periodic chains.

Finally, having (A.8) at hand, one can find by diagonalization of the  $2 \times 2$  Hamiltonian that the energy gap for excitation of the pair of  $\pm k$  fermionic modes is

$$4\sqrt{g^2 - 2g \cos(k) + 1}. \tag{A.10}$$

The smallest value of that gap, in each of the parity subspaces, is the dynamical gap  $\Delta_\pm$ —see also figure 2. Thereby,

$$\Delta_+ = 4\sqrt{g^2 - 2g \cos(\pi/N) + 1}, \quad \Delta_- = 4\sqrt{g^2 - 2g \cos(2\pi/N) + 1}. \quad (\text{A.11})$$

## Appendix B. Diagonalization and time evolution of Ising chains with open boundaries

We will briefly summarize here technicalities related to diagonalization of the Ising chain with open boundaries, computation of its longitudinal magnetization, and its time evolution.

### B.1. Diagonalization

We follow here [46] providing an early take on this subject. The diagonalization begins with Jordan–Wigner spin-to-fermion mapping (A.1) transforming Hamiltonian (33) to the following quadratic form

$$\begin{aligned} \tilde{H} &= \Psi^\dagger \mathcal{H} \Psi, \\ \Psi^\dagger &= (c_1^\dagger \dots c_N^\dagger c_1 \dots c_N), \end{aligned} \quad (\text{B.1})$$

$$\mathcal{H} = \begin{pmatrix} A & B \\ -B & -A \end{pmatrix},$$

where  $A$  and  $B$  are  $N \times N$  tridiagonal matrices

$$\begin{aligned} A_{ij} &= g \delta_{i,j} - 1/2 \delta_{i,j+1} - 1/2 \delta_{i+1,j}, \\ B_{ij} &= 1/2 \delta_{i,j+1} - 1/2 \delta_{i+1,j}. \end{aligned} \quad (\text{B.2})$$

We mention in passing that we have corrected a misprint from [46] in the expression for  $B_{ij}$ .

Next, for every value of the magnetic field  $g$ , one can perform the Bogolubov transformation

$$\begin{aligned} \Psi &= \beta \Gamma, \\ \Gamma^\dagger &= (\gamma_1^\dagger \dots \gamma_N^\dagger \gamma_1 \dots \gamma_N) \end{aligned} \quad (\text{B.3})$$

choosing real orthogonal matrix  $\beta$  in such a way that (B.1) is diagonal. This leads to (34) and the related equations (35)–(37). Two remarks are in order now.

First, as a self-consistency check of our calculations, we have verified that energies of single-particle excitations, which we have obtained from numerical diagonalization of  $\mathcal{H}$ , very well agree with the results coming from (36) combined with (37).

Second, the symmetry-breaking gap can be analytically calculated from (37) only at the critical point, where

$$\delta(g = 1) = 4 \sin \frac{\pi}{4N + 2} \approx \frac{\pi}{N}. \quad (\text{B.4})$$

This is about twice larger than the symmetry-breaking gap in the periodic chain (11).

### B.2. Equilibrium longitudinal magnetization

To compute the equilibrium longitudinal magnetization  $M_x^{\text{eq}}$ , we evaluate (38) in the state

$$\frac{|GS\rangle + \gamma_1^\dagger |GS\rangle}{\sqrt{2}}, \tag{B.5}$$

where  $|GS\rangle$  is the ground state annihilated by all  $\gamma_i$  operators. This leads to the following expression for the longitudinal magnetization after employment of Wick's theorem

$$M_x^{\text{eq}} = \langle GS | \gamma_1 \sigma_{N/2}^x | GS \rangle. \tag{B.6}$$

The operator  $\gamma_1 \sigma_{N/2}^x$  can be conveniently written as

$$\gamma_1 \sigma_{N/2}^x = \gamma_1 a_{N/2} b_{N/2-1} a_{N/2-1} \dots b_1 a_1, \quad a_i = c_i + c_i^\dagger, \quad b_i = c_i - c_i^\dagger. \tag{B.7}$$

Using Wick's theorem again, one can show that

$$\langle GS | \gamma_1 \sigma_{N/2}^x | GS \rangle = \text{Pf}(G),$$

$$G = \begin{pmatrix} 0 & \langle \gamma_1 a_{N/2} \rangle & \langle \gamma_1 b_{N/2-1} \rangle & \langle \gamma_1 a_{N/2-1} \rangle & \dots & \langle \gamma_1 a_1 \rangle \\ & 0 & \langle a_{N/2} b_{N/2-1} \rangle & \langle a_{N/2} a_{N/2-1} \rangle & \dots & \langle a_{N/2} a_1 \rangle \\ & & 0 & \langle b_{N/2-1} a_{N/2-1} \rangle & \dots & \langle b_{N/2-1} a_1 \rangle \\ & & & & & \vdots \\ & & & & & 0 \end{pmatrix}, \tag{B.8}$$

where Pf stands for Pfaffian, the lower triangle of the  $G$  matrix can be obtained by the relation  $G = -G^T$ , and the expectation values are calculated in the ground state  $|GS\rangle$ . Pfaffians of skew-symmetric matrices can be efficiently computed using Hausholder transformation [47].

### B.3. Time evolution

We work in the Heisenberg picture. Our evolutions start at time  $t_0$  from the equal superposition of the two lowest-energy eigenstates of  $\tilde{H}[g(t_0)]$

$$\frac{|GS[g(t_0)]\rangle + \gamma_1^\dagger |GS[g(t_0)]\rangle}{\sqrt{2}}. \tag{B.9}$$

Two remarks are in order now.

First, initial state (B.9) for time evolution is constructed in the same way as for evolutions in periodic chains. In particular, the two states in (B.9) have different parities. In fact, it is perhaps worth to say again that Hamiltonian  $\tilde{H}$  for the Ising chain with open boundaries commutes with the parity operator. Therefore, its eigenstates can be labeled with the  $\pm 1$  parities. Moreover, expectation values of the  $\sigma_i^x$  operators in all

eigenstates of  $\tilde{H}$  are zero. The very same properties are found in periodic chains, which have been discussed in sections 2–4.

Second, using quench protocol (4), one gets  $g(t_0 = -g_f\tau_Q) = 0$  and the initial state (B.9) is given by (3). It is numerically convenient for us, however, to begin evolutions from the slightly non-zero  $g$ , which we do by choosing  $t_0$  such that  $g(t_0) = 0.001$ .

Time-dependent longitudinal magnetization (38) is then expressed as

$$M_x(t) = \text{Re}\langle GS[g(t_0)] | \gamma_1 \sigma_{N/2}^x(t) | GS[g(t_0)] \rangle, \quad (\text{B.10})$$

where the operator  $\gamma_1$  is defined at time  $t_0$ . The matrix element in this equation can be computed just as (B.8) expect  $a_i$  and  $b_i$  operators are now time dependent. Thus, we need to know their time evolution, which can be extracted from

$$\Psi(t) = U(t)\Psi(t_0), \quad (\text{B.11})$$

where the  $N \times N$  unitary matrix  $U(t)$  can be obtained by solving

$$\frac{d}{dt}U(t) = -2i\mathcal{H}U(t) \quad (\text{B.12})$$

with the initial condition  $U(t_0) = \mathbb{1}$ . Equation (B.12) can be derived from the Heisenberg equations for the  $c_i(t)$  and  $c_i^\dagger(t)$  operators. We solve it numerically with the Suzuki-Trotter method of order two with the time step smaller or equal to 0.01 [48]. We have checked that such a procedure produces well-converged results.

Having  $U(t)$  and the Bogolubov matrix  $\beta$  at the time  $t_0$ , we can relate  $c_i(t)$  and  $c_i^\dagger(t)$  operators to  $\gamma_i$  and  $\gamma_i^\dagger$  appearing in the diagonal form of  $\tilde{H}[g(t_0)]$ . Namely,

$$\Psi(t) = W(t)\Gamma, \quad W(t) = U(t)\beta, \quad (\text{B.13})$$

where the matrix  $W$  has the following structure

$$W = \begin{pmatrix} C & D \\ \overline{D} & \overline{C} \end{pmatrix} \quad (\text{B.14})$$

with  $C$  and  $D$  being  $N \times N$  complex matrices. Transformation (B.13) can be used to compute all correlation functions, from time-dependent version of (B.8), needed for getting (B.10). For example, after straightforward manipulations one can show that

$$\langle a_i a_j \rangle = \sum_{k=1}^N (C_{ik}D_{jk} + C_{ik}\overline{C_{jk}} + \overline{D_{ik}}D_{jk} + \overline{D_{ik}}\overline{C_{jk}}). \quad (\text{B.15})$$

## References

- [1] Sachdev S 2011 *Quantum Phase Transitions* (Cambridge: Cambridge University Press)
- [2] Continentino M 2017 *Quantum Scaling in Many-Body Systems: an Approach to Quantum Phase Transitions* 2nd edn (Cambridge: Cambridge University Press)
- [3] Sachdev S and Keimer B 2011 *Phys. Today* **64** 29
- [4] Lewenstein M, Sanpera A, Ahufinger V, Damski B, Sen De A and Sen U 2007 *Adv. Phys.* **56** 243
- [5] Dziarmaga J 2005 *Phys. Rev. Lett.* **95** 245701
- [6] Zurek W H, Dorner U and Zoller P 2005 *Phys. Rev. Lett.* **95** 105701
- [7] Polkovnikov A 2005 *Phys. Rev. B* **72** 161201
- [8] Mostame S, Schaller G and Schützhold R 2007 *Phys. Rev. A* **76** 030304

- [9] Barankov R and Polkovnikov A 2008 *Phys. Rev. Lett.* **101** 076801
- [10] Mondal S, Sengupta K and Sen D 2009 *Phys. Rev. B* **79** 045128
- [11] Patanè D, Amico L, Silva A, Fazio R and Santoro G E 2009 *Phys. Rev. B* **80** 024302
- [12] Cincio L, Dziarmaga J, Rams M M and Zurek W H 2007 *Phys. Rev. A* **75** 052321
- [13] Sengupta K and Sen D 2009 *Phys. Rev. A* **80** 032304
- [14] Das A 2010 *Phys. Rev. B* **82** 172402
- [15] Kolodrubetz M, Clark B K and Huse D A 2012 *Phys. Rev. Lett.* **109** 015701
- [16] Francuz A, Dziarmaga J, Gardas B and Zurek W H 2016 *Phys. Rev. B* **93** 075134
- [17] Russomanno A, Sharma S, Dutta A and Santoro G E 2015 *J. Stat. Mech.* P08030
- [18] Puskarov T and Schuricht D 2016 *SciPost Phys.* **1** 003
- [19] Lorenzo S, Marino J, Plastina F, Palma G M and Apollaro T J G 2017 *Sci. Rep.* **7** 5672
- [20] Białończyk M and Damski B 2018 *J. Stat. Mech.* 073105
- [21] del Campo A 2018 *Phys. Rev. Lett.* **121** 200601
- [22] Rams M M, Dziarmaga J and Zurek W H 2019 *Phys. Rev. Lett.* **123** 130603
- [23] Gross C and Bloch I 2017 *Science* **357** 995
- [24] Makhlov V, Satoor T, Evrard A, Chalopin T, Lopes R and Nascimbene S 2019 *Phys. Rev. Lett.* **123** 120601
- [25] Lieb E, Schultz T and Mattis D 1961 *Ann. Phys., NY* **16** 407
- [26] Pfeuty P 1970 *Ann. Phys.* **57** 79
- [27] Giuliani G F and Vignale G 2005 *Quantum Theory of the Electron Liquid* (Cambridge: Cambridge University Press)
- [28] Damski B and Rams M M 2014 *J. Phys. A* **47** 025303
- [29] Damski B 2005 *Phys. Rev. Lett.* **95** 035701
- [30] Kibble T W B 1980 *Phys. Rep.* **67** 183
- [31] Zurek W H 1996 *Phys. Rep.* **276** 177
- [32] del Campo A, Kibble T W B and Zurek W H 2013 *J. Phys.: Condens. Matter* **25** 404210
- [33] del Campo A and Zurek W H 2014 *Int. J. Mod. Phys. A* **29** 1430018
- [34] Dziarmaga J 2010 *Adv. Phys.* **59** 1063
- [35] Wolfram Research, Inc. 2016 *Mathematica, Version 11.0* (Champaign, IL: Wolfram Research, Inc.)
- [36] Korenblit S *et al* 2012 *New J. Phys.* **14** 095024
- [37] Cabrera G G and Jullien R 1987 *Phys. Rev. B* **35** 7062
- [38] Prośniak O A 2019 *Phys. Scr.* **94** 085201
- [39] Bernien H *et al* 2017 *Nature* **551** 579
- [40] Zhang J, Pagano G, Hess P W, Kyprianidis A, Becker P, Kaplan H, Gorshkov A V, Gong Z-X and Monroe C 2017 *Nature* **551** 601
- [41] Keesling A *et al* 2019 *Nature* **568** 207
- [42] Porras D and Cirac J I 2004 *Phys. Rev. Lett.* **92** 207901
- [43] Schauss P 2018 *Quantum Sci. Technol.* **3** 023001
- [44] Harris R *et al* 2018 *Science* **361** 162
- [45] Gardas B, Dziarmaga J, Zurek W H and Zwolak M 2018 *Sci. Rep.* **8** 4539
- [46] Young A P 1997 *Phys. Rev. B* **56** 11691
- [47] Wimmer M 2012 *ACM Trans. Math. Softw.* **38** 30
- [48] Hatano N and Suzuki M 2005 Finding exponential product formulas of higher orders Quantum Annealing and Other Optimization Methods Das A, Chakrabarti B (Berlin: Springer) pp 37–68